

Enhanced photothermal response near the buckling bifurcation in 2D nanomechanical resonators

Hanqing Liu,^{*,†} Gabriele Baglioni,[‡] Carla B. Constant,[¶] Herre S. J. van der Zant,[‡] Peter G. Steeneken,^{†,‡} and Gerard J. Verbiest^{*,†}

[†]*Department of Precision and Microsystems Engineering, Delft University of Technology, Lorentzweg 1, 2628 CD Delft, The Netherlands*

[‡]*Kavli Institute of Nanoscience, Delft University of Technology, 2628 CJ Delft, The Netherlands*

[¶]*Instituto de Ciencia Molecular (ICMol), Universitat de Valencia, Paterna 46980, Spain*

E-mail: HanqingLiu@tudelft.nl; G.J.Verbiest@tudelft.nl

Abstract

The dynamics of ultrathin membranes made of two-dimensional (2D) materials is highly susceptible to stress. Although the dynamics of such membranes under tensile stress has been thoroughly studied, their motion under compressive stress, particular in the buckled state has received less attention. Here, we study the dynamics of 2D nanomechanical resonators made of FePS₃, 2H-TaS₂ and WSe₂ membranes near the buckling bifurcation. Using an optomechanical method, we measure their resonant frequency and thermal transport while varying in-plane stress via membrane temperature and thermal expansion. The observed temperature dependence of the resonance frequency is well capture by a mechanical model, which allows us to extract the pre-strain, central deflection and boundary compressive stress of the membrane. Near the

buckling bifurcation, we observe a remarkable enhancement of up to $7\times$ the thermal signal in the fabricated devices, demonstrating the extremely high force-sensitivity of the membranes near this point. The presented results provide insights into the effects of buckling on the dynamics of free-standing 2D materials and thereby open up opportunities for the realization of 2D resonant nanomechanical sensors with buckling-enhanced sensitivity.

Keywords

2D nanomechanical resonator, Mechanical buckling model, Resonance frequency, Thermal expansion

INTRODUCTION

A flat mechanical plate subjected to a sufficiently high in-plane compressive stress becomes unstable, as its out-of-plane stiffness gradually reduces to zero.¹ When this happens, the plate experiences a buckling bifurcation. Even the slightest imperfection in the device, like a very small initial deformation, can determine whether the plate buckles up or downward. This high sensitivity to initial conditions offers exciting prospects, both for studying material properties^{2,3} and for realizing new sensing applications.⁴ Therefore there has been a growing recent interest for buckling in nano-electromechanical systems (NEMS) and resonators such as phononic waveguides,⁵ carbon nanotubes⁶ and SiN_x drumheads,⁷ showing reversible control of signal transmission, high sensitive switching, as well as remarkable nonlinear effects and high tunability of resonance frequencies. These properties of buckled resonators make them very relevant for applications as actuators, sensors, and energy harvesters.^{8,9}

Nanomechanical resonators made of free-standing 2D materials are stiff within the plane, due to their high Young's modulus, but extremely flexible out-of-plane due to their atomic thickness.¹⁰⁻¹² As a result, free-standing 2D materials buckle at relatively low compressive

stress values and thereby present an ideal platform for studying the buckling bifurcation in nanoscale systems. In fact, the buckling bifurcation provides a sensitive method to determine the bending rigidity of 2D materials.^{2,13} However, most of the work on 2D NEMS resonators has focused on flat 2D mechanical resonators under tensile stress, because these can be more reproducibly fabricated^{14,15} and more easily modeled. Moreover, the experimental detection of the buckling bifurcation in 2D NEMS remains difficult, as it requires a methodology to induce symmetric in-plane compression in suspended 2D materials while measuring their mechanical motion with high spatial resolution.

In this letter, we study the effect of the buckling bifurcation on the dynamics of optothermally driven 2D nanomechanical resonators. By varying temperature, the membranes expand, causing a compressive stress that triggers the membranes to deflect out-of-plane. Interestingly, this bifurcation does not only cause a large change in the temperature-dependent resonance frequency, but also gives rise to a significant enhancement of the amplitude of the resonators, both when driven on-resonance and off-resonance. To account for these observations and relate them to the device parameters, we fit a mechanical buckling model to the experiments that quantifies prestrain, central membrane deflection, and boundary compressive stress of the membrane. Based on the model we attribute the enhanced photothermal response to a significantly reduced out-of-plane stiffness at buckling transition. The high response to force of 2D resonators near the buckling bifurcation might be utilized in future designs of 2D NEMS devices and sensors like microphones and pressure sensors that require ultimate sensitivity limit.

RESULTS AND DISCUSSION

We fabricated 2D nanomechanical resonators by transferring exfoliated 2D flakes over etched circular cavities with a depth of $d = 285$ nm and varying radius r in a Si/SiO₂ substrate (Methods). In total, we fabricated three FePS₃ devices D1–D3, a 2H-TaS₂ device D4,

Table 1: Characteristics of fabricated devices D1–D5, including radius r , thickness t , Young’s modulus E , Poisson ratio ν , mass density ρ , initial resonance frequency $f_0(T_0)$, temperature at turning point T_t , resonance frequency at turning point f_t , pre-strain ϵ_0 (extracted from buckling model), pre-strain ϵ_0^* (obtained by AFM indentation), initial deflection z_0 (nm), and total strain at turning point ϵ_t . D1–D3, FePS₃ resonators; D1 and D2 are from the same FePS₃ nanoflake (see Fig. 1a); D4, 2H-TaS₂ resonator; D5, WSe₂ resonator.

	r (μm)	t (nm)	E (GPa)	ν	ρ (g/cm ³)	$f_0(T_0)$ (MHz)	T_t (K)
D1	4	33.9	69.9	0.304	3.375	5.89	302.0
D2	4	33.9	70.3	0.304	3.375	5.52	303.0
D3	3	34.5	93.1	0.304	3.375	11.18	307.5
D4	3	10.5	201.6	0.350	6.860	24.06	336.0
D5	4	20.3	275.7	0.190	9.320	11.91	310.0

	f_t (MHz)	$\epsilon_0 \times 10^{-5}$	$\epsilon_0^* \times 10^{-5}$	z_0 (nm)	$\epsilon_t \times 10^{-5}$
D1	5.53	2.45 ± 0.08	2.82 ± 0.20	23.6 ± 0.1	-0.71
D2	3.97	6.94 ± 0.08	4.83 ± 0.30	11.7 ± 0.2	-6.01
D3	6.89	13.65 ± 0.10	11.18 ± 0.50	7.1 ± 0.2	-14.88
D4	21.14	35.54 ± 0.73	29.89 ± 0.30	59.9 ± 0.2	-2.48
D5	11.58	4.61 ± 0.39	3.43 ± 0.20	59.7 ± 0.2	-0.32

and a WSe₂ device D5. Figure 1a shows a schematic cross-section and a top view (optical microscope) of the fabricated FePS₃ devices D1 and D2 with $r = 4 \mu\text{m}$. Using tapping mode atomic force microscopy (AFM), we measure the height difference between the membrane and the Si/SiO₂ substrate. As Fig. 1b shows, we find a membrane thickness t of 33.9 nm for devices D1 and D2.

To determine the Young’s modulus E of the resonators, we indent the membrane centre by an AFM cantilever while measuring its deflection.¹⁶ We fit the applied force F versus indentation δ , as depicted in Fig. 1c (orange points), to a model for point-force loading of a circular plate given by $F = (\frac{16\pi D}{r^2}\delta) + n_0\pi\delta + Etq^3(\frac{\delta^3}{r^2})$, where $D = Et^3/(12(1 - \nu^2))$ is the bending rigidity of the membrane, ν is Poisson ratio, $n_0 = Et\epsilon_0/(1 - \nu)$ is the pre-tension in the membrane, and ϵ_0 is the built-in strain. From the fit (black line, Fig. 1c) we extract $E = 69.9$ GPa for device D1. The extracted prestrain and Young’s moduli of devices D2–D5 are listed in Table 1, which are in good agreement to values reported in the literature.^{17–19}

To probe the thermodynamic properties of the fabricated devices, we use a laser inter-

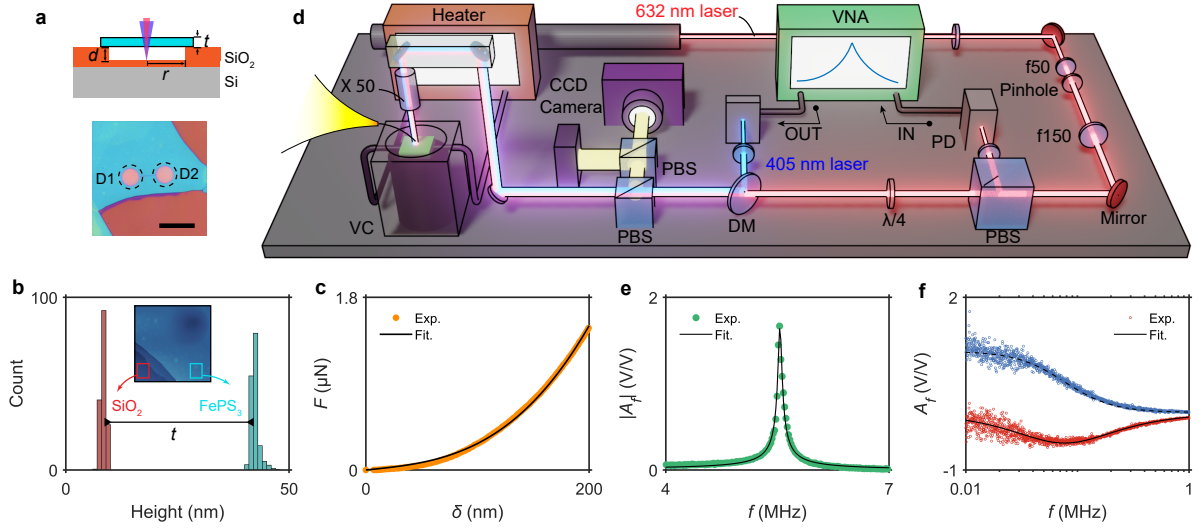


Figure 1: Characterization of FePS₃ device D1. (a) Top, cross-section of a FePS₃ membrane suspended on the etched Si/SiO₂ substrate. Bottom, optical images of the fabricated FePS₃ devices D1 and D2. Scale bar is 15 μm. (b) Height histogram of substrate (red), as well as FePS₃ membrane (cyan), measured by AFM. Insert, AFM scanning image on the boundary of FePS₃ flake. (c) AFM indentation results for device D1 (orange points), where the Young's modulus E of membrane is extracted by fitting the measured force F to the cantilever deflection δ (black line). (d) Setup for detecting the thermodynamic properties of 2D nanomechanical resonators, where the chip is fixed inside a vacuum chamber (VC). VNA, vector network analyzer; PBS, polarized beam splitter; PD, photo diode; DM, dichroic mirror. (e) Absolute signal $|A_f|$ around the resonance frequency (green points) for device D1, which is fitted with a harmonic oscillator model to extract the resonance frequency f_0 and its quality factor Q (black line). (f) Signal A_f measured in the kHz regime, including imaginary (red points) and real parts (blue points), which are fitted with Eq. 1 to obtain the thermal time constant τ and thermal expansion amplitude A_{th} of the resonator (black lines).

ferometer (see Methods).²⁰ As shown in Fig. 1d, we place the samples in a vacuum chamber with a pressure below 10^{-5} mbar during the measurements. A power-modulated diode laser ($\lambda = 405$ nm) photothermally actuates the resonator, while the reflection of a He-Ne laser ($\lambda = 632$ nm) from the Fabry-Perot cavity with the suspended membrane captures its motion. The reflection is measured by a photodetector (PD) and processed by a Vector Network Analyzer (VNA) and then converted to the response amplitude A_f of the resonator in the frequency domain. Figure 1e shows the measured frequency response around the fundamental resonance (green points) and a fit to a harmonic oscillator model (black line), given by $A_f = \frac{A_{\text{res}}f_0^2}{Q\sqrt{(f_0^2-f^2)^2+(f_0f/Q)^2}}$, where f_0 is resonance frequency, A_{res} is the vibrating amplitude at resonance and Q is quality factor. We extract $f_0 = 5.57$ MHz and $Q = 195.93$ for device D1. In addition to the fundamental resonance, we observe a thermal peak in the imaginary part of the response in the 10-100 kHz regime (see Fig. 1f), which we attribute to the thermal expansion of the membrane that is thermally delayed with respect to the power of the modulated laser.^{21,22} By solving the in-plane heat equation in membrane, A_f of the thermal signal can be expressed as

$$A_f = \frac{A_{\text{th}}}{i2\pi f\tau + 1}, \quad (1)$$

where A_{th} and τ are the thermal expansion amplitude and thermal time constant of the membrane, respectively. We extract A_{th} and τ by fitting the measured A_f (imaginary part) with Eq. 1, as depicted in Fig. 1f (drawn line). Here, $|A_{\text{th}}| = 1.75$ V/V and the thermal signal in the imaginary part of A_f is located at around 76.63 kHz, which corresponds to $\tau = (2\pi \times 76.63 \text{ kHz})^{-1} = 2.09 \mu\text{s}$.

Figure 2a shows $|A_f|$ as a function of actuation frequency and temperature (in the range from 300 to 316 K) for device D1. Interestingly, the resonance frequencies, including fundamental mode (indicated by the blue arrows) and second mode, first decrease and then increase with increasing temperature. We attribute this behavior to the mechanical buckling of the nanomechanical resonators under critical compressive loading, which has been reported before in carbon nanotube resonator⁶ and arch MEMS devices.²³ In fact, the bulk

thermal expansion coefficients (TEC), α_m , of the measured 2D materials in this work are much larger than the TEC α_{Si} of the Si/SiO₂ substrate. Hence, heating induces compressive strain in the resonators and buckling is a natural consequence.

Due to the buckling, we cannot use the standard equation for the resonance frequency of a pre-tensioned plate or membrane for further analysis. Therefore, we use a mechanical buckling model for clamped circular membranes, as illustrated in Fig. 2b. From the stored elastic energy in the resonator (see SI section 1 and refs.²⁴⁻²⁶), we obtain an expression of the fundamental resonance frequency f_0 under thermally induced strain:

$$f_0(T) = \frac{c_1}{2\pi r} \sqrt{\frac{E}{\rho(1-\nu^2)} \left(\epsilon_0 + \Delta\epsilon(T) + \frac{c_2 z(T)^2}{r^2} + \frac{c_3 t^2}{r^2} \right)}, \quad (2)$$

where ϵ_0 and $\Delta\epsilon$ are the pre-strain and thermally induced compressive strain in the membrane, respectively, ρ is the mass density, and z is the central deflection of the membrane. Both $\Delta\epsilon$ and z depend on T . The total strain in the membrane, $\epsilon(T)$, is given by $\epsilon(T) = \epsilon_0 + \Delta\epsilon(T)$. The constants $c_1 = 2.0367$, $c_2 = 2.7758$ and $c_3 = 1.5147$ in Eq. 2 depend on the mode shape of the membrane (see derivations in SI section 1). In contrast to the standard equation for the resonance frequency of a pre-tensioned plate or membrane, we now find that not only the pre-tension ϵ_0 and the bending rigidity (D/t is related to $c_3 t^2/r^2$) determine $f_0(T)$, but also the thermally-induced compression $\Delta\epsilon$ and the center deflection z of the membrane.

To find the relation between $\Delta\epsilon$ and z , we consider a uniformly-clamped plate as depicted in Fig. 2b. The axial displacement of the membrane, induced by heating, comprises of two components: the axial compression on the boundary and the geometrical deformation of the membrane (see detailed derivation in SI section 1). Accordingly, we obtain:

$$-\Delta\epsilon = \frac{k_1 t^2 (1 + \nu)}{12 r^2} \left(1 - \frac{z_0}{z} \right) + \frac{\pi^2}{8 r^2} (z^2 - z_0^2), \quad (3)$$

where z_0 is the initial deflection of the membrane at room temperature and $k_1 = 14.68$ is

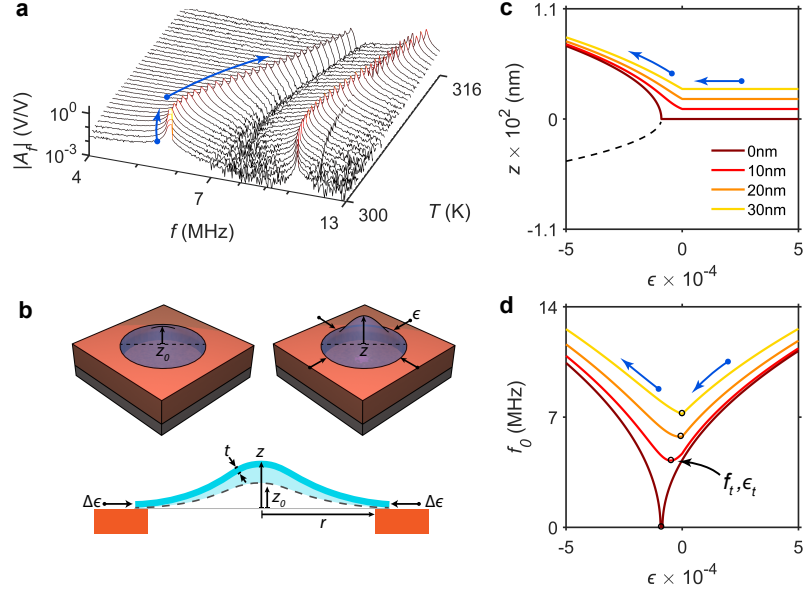


Figure 2: Mechanical buckling model for 2D nanomechanical resonators. (a) Mechanical response $|A_f|$ of FePS₃ device D1 as a function of frequency f and temperature T . The fundamental resonance frequency f_0 first decreases with increasing T up to a temperature T_t , after which f_0 also increases (blue arrows). (b) Mechanical buckling illustration for a clamped circular membrane, where a compressive load $\Delta\epsilon$ from the boundary of membrane causes a central deflection z . (c) z versus the total strain ϵ in the membrane estimated by Eq. 3, using the parameters $r = 4 \mu\text{m}$, $E = 100 \text{ GPa}$, $t = 30 \text{ nm}$, $\epsilon_0 = 5 \times 10^{-4}$, $\rho = 3375 \text{ kg/m}^3$ and $\nu = 0.304$. ϵ is given as $\epsilon = \Delta\epsilon + \epsilon_0$. Lines, results under different values of initial deflection z_0 of the membrane. Dotted line, supercritical bifurcation at the critical buckling load when $z_0 = 0$. (d) f_0 of the resonator versus ϵ . Black hollow dots, resonance frequency f_t at the turning point.

the first critical buckling factor taken from literature.²⁷ The minus in front of $\Delta\epsilon$ indicates that $\Delta\epsilon(T)$ opposes ϵ_0 . By substituting the parameters $r = 4 \text{ }\mu\text{m}$, $E = 100 \text{ GPa}$, $t = 30 \text{ nm}$, $\epsilon_0 = 5 \times 10^{-4}$, $\rho = 3.375 \text{ g/cm}^3$ and $\nu = 0.304$ into Eq. 3, we can evaluate z as a function of $\Delta\epsilon$ for different z_0 . As plotted in Fig. 2c for $z_0 > 0$, z first remains constant at z_0 and then increases once the total strain ϵ is compressive ($\epsilon_0 + \Delta\epsilon \leq 0$). The dotted black line in Fig. 2c represents a supercritical bifurcation at the critical buckling load when $z_0 = 0$. This physically indicates that $z_0 = 0$ becomes an unstable equilibrium, that will either buckle up or down when it is slightly perturbed. For nonzero z_0 , the membrane always buckles in the direction of the initial deflection. In order to investigate the effect of buckling on the resonance frequency f_0 , we substitute the relation between z and $\Delta\epsilon$ into Eq. 2. This results in a relation between f_0 and $\Delta\epsilon$ that depends on the value of z_0 , as plotted in Fig. 2d. When decreasing the total strain ϵ by decreasing $-\Delta\epsilon$, f_0 reduces to a minimal value (the turning point) and then starts to increase. At this turning point, the minimum resonance frequency f_t of the resonator is reached (marked as hollow dots in Fig. 2d) at a strain ϵ_t . Note that for nonzero z_0 , ϵ_t is different from the point where $\epsilon = 0$. Both the experimental curves in Fig. 2 and the theoretical curves in Fig. 2d show a clear frequency minimum, which we take as qualitative evidence for the occurrence of buckling in the 2D resonators.

Let us now quantify ϵ and z as a function of T for FePS₃ device D1, using a model that follows the flow chart depicted in Fig. 3a. First, we need to determine the values of z_0 and ϵ_0 in the mechanical buckling model. For this, we use two specific features in the measured f_0 versus T data (Fig. 3b), which are:

Case i: at the initial point, $T = T_0$, $\Delta\epsilon(T_0) = 0$ and $z(T_0) = z_0$,

Case ii: at the turning point, $T = T_t$, $\frac{df_0}{dT}|_{T=T_t} = 0$.

Assuming the Young's modulus of membrane remains constant within the probed temperature range,²⁸ z_0 and ϵ_0 can be extracted from the conditions (i) and (ii) when using the measured values of $f_0(T_0) = 5.89 \text{ MHz}$ (for $T = 300 \text{ K}$) and $f_t(T_t) = 5.53 \text{ MHz}$. The

solutions for z_0 and ϵ_0 (see derivation in SI section 1) are given by:

$$\begin{cases} \frac{c_t(f_t^2 - f_0^2(T_0))}{\frac{c_2}{r^2} - \frac{\pi^2}{8r^2}} = 3\sqrt[3]{\eta^2 z_0^2} - 2\eta - z_0^2, \\ c_t f_0^2(T_0) = \epsilon_0 + \frac{c_2 z_0^2}{r^2} + \frac{c_3 t^2}{r^2}, \end{cases} \quad (4)$$

where the constants $1/c_t = (\frac{c_1}{2\pi r})^2 \frac{E}{\rho(1-\nu^2)}$ and $\eta = \frac{k_1 t^2(1+\nu)}{24(c_2 - \pi^2/8)}$. Using Eq. 4, we obtain $z_0 = 23.6$ nm and $\epsilon_0 = 2.45 \times 10^{-5}$ for device D1 (Table 1). The obtained value of ϵ_0 is within the range of values reported in the literature^{22,26,29} and is in agreement with the one extracted by AFM indentation (Fig. 1c). By substituting the obtained z_0 and ϵ_0 into Eq. 3, we extract ϵ as a function of T (see Fig. 3c). The strain ϵ_t at T_t is compressive with a value of -0.71×10^{-5} . We find that $-\epsilon$ becomes more than 10 times larger than the pre-strain ϵ_0 by heating the membrane by only 16 K. The total strain in the FePS₃ membrane thus changes from the initial tensile strain to a strong compressive strain.

To validate the extracted $\epsilon(T)$, we determine the TEC of the membrane α_m . Using the TEC of the substrate α_{Si} , we can use the relation $\frac{d\Delta\epsilon}{dT} = -(\alpha_m - \alpha_{Si})$ to determine α_m .¹⁸ We thus fit this relation to the obtained ϵ as shown in Fig. 3c (drawn line) and find $\alpha_m = 2.4 \times 10^{-5}$ K⁻¹. This value for α_m is in good agreement with values reported in the literature for FePS₃.³⁰

To experimentally validate the extracted $z(T)$ from the buckling model, we use a white light interferometer to image the surface profile of the suspended FePS₃ membranes as a function of temperature. As shown in Fig. 3d, we observe from the height profiles (black arrows, top panel) that the membrane deformation increases as T goes up (bottom panel). As a measure for $z(T)$, we take the difference between the maximum and minimum height for two height profiles and take the average value. The extracted $z(T)$ (points) for device D1 quantitatively matches the estimated $z(T)$ from $f_0(T)$ (drawn line), as plotted in Fig. 3e. We attribute the deviation at low T to the air pressure in the cavity underneath the resonator, since the measurements with the white light interferometer were carried out at ambient

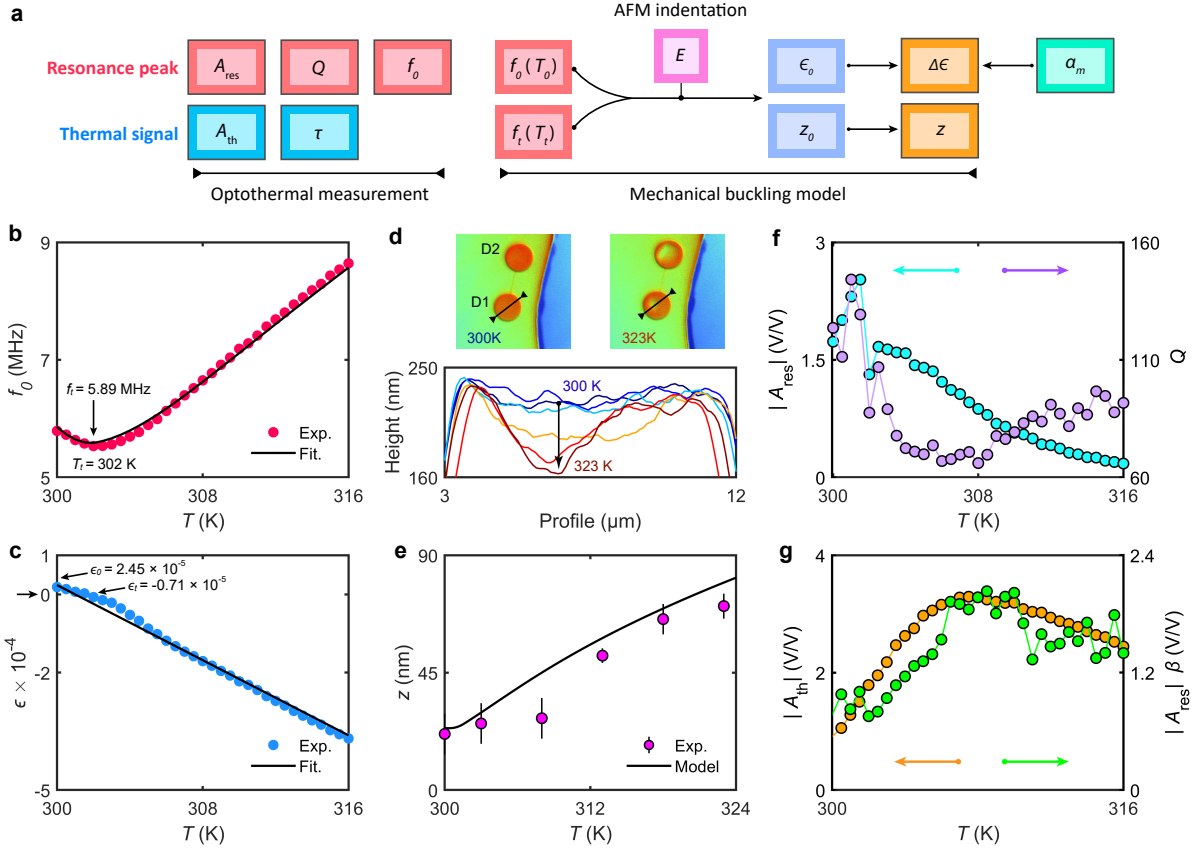


Figure 3: Temperature-dependent optomechanical measurement on FePS₃ device D1. (a) Flow chart to determine the induced strain $\Delta\epsilon$ and central deflection z of the membranes. The parameters in a gray frame are T -dependent. (b) Fundamental resonance frequency f_0 versus T (red points). The minimum in f_0 is indicative of the temperature T_t at around 302 K. Drawn line, f_0 versus T fitted with the mechanical buckling model to the measurement, using the TEC of FePS₃ $\alpha_m = 2.4 \times 10^{-5} \text{ K}^{-1}$. (c) Total strain ϵ versus T in the membrane, obtained from Eq. 2 using the measured f_0 and the extract z_0 and ϵ_0 . The strain ϵ_t at the turning point is -0.71×10^{-5} . Drawn line, fitting result with the given constant α_m . (d) Top, images of FePS₃ flake under white light interferometry. Bottom, surface profile of the membrane as T increases (corresponding to the black arrow in top insert). (e) Measured central deflection $z(T)$ of device D1 (points), which agrees well with the estimation of Eq. 3 (drawn line). Error bar originates from the selected two scanning profiles. (f) Amplitude of resonance peak $|A_{\text{res}}|$ (cyan points) and quality factor Q (purple points) versus T for device D1, respectively. (g) Measured amplitude $|A_{\text{th}}|$ of thermal signal versus T (orange points), which shows comparable variation with the estimation using $|A_{\text{res}}|/\beta$ (green points).

conditions. Similar results for device D2 can be found in Fig. S2b. These measurements thus confirm that both devices D1 and D2 exhibit mechanical buckling and validates the extracted $z(T)$ using the buckling model.

As the effective spring constant $k_s = m_{\text{eff}}(2\pi f_0)^2$ of the fundamental mode of a resonator is minimal for the lowest resonance frequency f_0 , we now focus on the vibration amplitude of the membrane. Figure 3f plots the amplitude $|A_{\text{res}}|$ and Q of the resonance peak as a function of T for device D1. We indeed observe a maximum in $|A_{\text{res}}|$ exactly located at $T_t = 302$ K. Surprisingly, the maximum of thermal signal, $|A_{\text{th}}|$, appears at around $T = 307$ K (Fig. 3g). To understand this, we use the theoretical relation $|A_{\text{th}}| = |A_{\text{res}}|\beta$, where the factor β depends on $f_0(T)$, $Q(T)$ and $\tau(T)$ (see SI section 3). As plotted in Fig. 3g, the estimated $|A_{\text{th}}|$ versus T (green points) shows the same trend as the measurement (orange points). The quantity $|A_{\text{th}}|$ are a factor 1.7 smaller than the measured ones. We attribute this to the optical non-linearity in the read-out of the Fabry-Perot cavity.³¹

We also observe the thermally induced buckling during the optomechanical measurements on devices D2–D5, as shown in Fig. 4a. The frequency tuning of these devices is explained with the built buckling model for 2D resonators. For all devices D2–D5, we extract z_0 and ϵ_0 using Eq. 4 and the measured $f_0(T_0)$ and f_t (see Table 1). The obtained values of ϵ_0 are comparable to the results obtained by AFM indentation. We then substitute the extracted z_0 and ϵ into Eq. 2 to estimate f_0 versus T (drawn lines, Fig. 4a). The deviation between the measured and estimated $f_0(T)$, especially at high T , suggests that α_m or E of the membrane is T -dependent. Figure 4b depicts the measured amplitude $|A_{\text{res}}(T)|$ and $Q(T)$ of the resonance peak for devices D2–D5. Similar to what was observed for device D1, the maximum of $|A_{\text{res}}|$ coincides with the minimum in resonance frequency. The measured $|A_{\text{th}}(T)|$ also show remarkable enhancements of up to 7 folds near the buckling bifurcation for all devices D2–D5, which, as expected, has a similar temperature dependence as the amplitude at resonance $|A_{\text{res}}|$ (see Fig. 4c). Noticeably, $|A_{\text{th}}|$ of device D5 keeps increasing in the post-buckling regime, which we attribute to a variation in photothermal drive force

caused by a change in position z of the membrane, thereby changing the optical interference in the Fabry-Perot cavity.

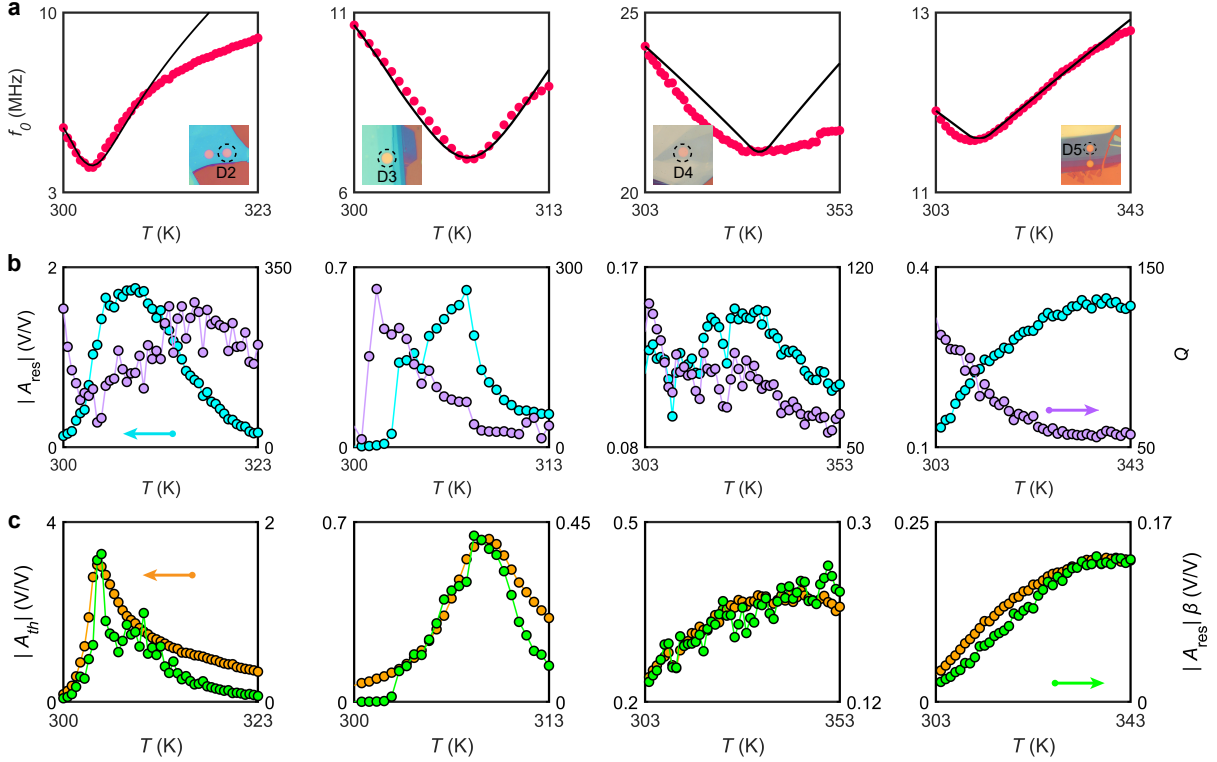


Figure 4: Experimental results of devices D2–D5 near buckling bifurcation. (a) Points, measured resonance frequency f_0 versus temperature T ; drawn lines, $f_0(T)$ estimated by Eq. 2 with the obtained z_0 and ϵ_0 in Table 1, fixing the TECs α_m as 3.9×10^{-5} , 3.3×10^{-5} , 1.2×10^{-5} and 4.7×10^{-6} for devices D2–D5, respectively. Inserts, optical images (top view) of the fabricated devices. (b) Amplitude $|A_{\text{res}}|$ (cyan points) and quality factor Q (purple points) of the resonance peak measured as the function of T . (c) Amplitude $|A_{\text{th}}|$ of thermal signal versus T . The estimation using $|A_{\text{res}}|\beta$ (green points) show comparable variation trend to the measurements (orange points) for all devices D2–D5, with a quantitative mismatch ranges from 1.46 to 1.83.

We expect similar behaviour might be found in membranes made of other 2D materials and in materials like SiN_x . Even for materials with a negative TEC such as graphene, buckling might occur if it is cooled down and the initial tensile stress is low enough. A key assumption in Eqs. 2 and 3 is a uniform compressive force at the boundary of the membrane and a constant Young’s modulus over the measured temperature range. In reality, inhomogeneities due to uneven adhesion between membrane and substrate could lead to

multiple smaller corrugations and wrinkles superimposed in the membrane when buckling occurs. This potential limitation, which we did not observe for the devices studied in this work, deserves future study as the buckled mode shape as well as the Young’s modulus depend on it.^{32,33} Possibly, the experimental quantification of the Young’s modulus for each device with the AFM, as we did in this work (Fig. 1c), irons out some of the corrugations and wrinkles.

Despite the fact that the temperature-dependence of resonance frequency has been investigated in earlier works on 2D membranes,^{34–36} mechanical buckling has not been reported yet. It seems that one study on MoS₂ resonators might have almost reached the buckling point ($\frac{df_0}{dT} \rightarrow 0$) at around 373 K.³⁴ In this work it was relatively straightforward to reach the buckling bifurcation due to the large TECs of the selected 2D materials. It is of interest to speculate on the ultimate limits of buckling induced resonance frequency decrease. As indicated in Fig. 2d, theoretically it might be possible to have the resonance frequency approaching zero for an initial deflection $z_0 = 0$ nm. However, in practice it will be difficult to reach that point. Nevertheless, by making the membranes flatter and with low pre-stress, the zero resonance frequency might be approached, which allows for an extremely high tunability ($\delta f_0/f_t$) and therefore a high force, stress and temperature sensitivity of f_0 near the minimum f_t . For such flat and low stress membranes, we expect the bending rigidity of 2D materials to dominate the performance and resonance frequency vs. temperature curve near the buckling bifurcation point.

Also from an application perspective, the thermally induced buckling in 2D nanomechanical resonators deserves further exploration. First, the frequency tuning is considerable. We obtain a sensitivity of 194.3 kHz/K for FePS₃ device D1 (Fig. 3b), which, when considering an accuracy of 1 kHz in determining f_0 , results in a temperature resolution of 5.1 mK. This value is comparable to state-of-the-art temperature sensors³⁷ and thus highlights the application buckled 2D resonators as bolometer³⁸ and NEMS resonant infrared detector.³⁹ Furthermore, precise control over the buckling bifurcation can be obtained by tailoring the

initial deflection of the membrane by applying, among others, electrostatic gating on the resonators,¹¹ a gas pressure difference,⁴⁰ or straining the resonators by MEMS actuators.⁴¹ The control over the membrane’s deformation also considerably modifies the capacitance between membrane and substrate, which could be employed for thermal switches.

In summary, we report the experimental observation of thermally-induced buckling in 2D nanomechanical resonators made of suspended FePS₃, 2H-TaS₂ and WSe₂ membranes. Using an optomechanical method, we detect their photothermal response as a function of temperature. A mechanical buckling model was developed to explain the observed turning of the resonance frequency with temperature, which allows us to determine the pre-strain, center deflection and thermally induced compression of the fabricated devices. We verified the enhancement of vibrating amplitude near buckling bifurcation, attributed to the decrease in out-of-plane stiffness. The gained insight not only advances the fundamental understanding of buckling bifurcation membranes made of 2D materials, but also enables pathways for buckling-enhanced designs and applications such as temperature detectors, thermoelectric and NEMS devices.

METHODS

Sample Fabrication. A Si wafer with 285 nm dry SiO₂ is spin coated with positive e-beam resist and exposed by electron-beam lithography. Afterwards, the SiO₂ layer without protection is completely etched using CHF₃ and Ar plasma in a reactive ion etcher. The edges of cavities are examined to be well-defined by scanning electron microscopy (SEM) and AFM. After resist removal, FePS₃, 2H-TaS₂ and WSe₂ nanoflakes are exfoliated by Scotch tape, and then separately transferred onto the substrate at room temperature through a deterministic dry stamping technique. Detailed descriptions of the FePS₃ and 2H-TaS₂ crystal growth and characterization can be found in earlier works.^{17,42}

Laser Interferometry Setup. We present temperature-dependent optomechanical measurements in a laser interferometry setup.¹⁸ The fabricated devices is fixed on a sample holder inside the vacuum chamber. A PID heater and a temperature sensor are connected with the sample holder, which allows to precisely monitor and control the temperature sweeping. A piezo-electric actuator below the sample holder is used to optimize the X-Y position of the sample to maintain both the blue and red laser in the center of the 2D resonators. We use a red and blue laser power of 0.9 and 0.13 mW respectively. Note we verified that the resonators vibrate in linear regime and the temperature raise due to self-heating is negligible.²¹

ASSOCIATED CONTENT

The Supporting Information is available free of charge at <https://pubs.acs.org/doi/xxxxxxx>.

AUTHOR INFORMATION

Author Contribution

H.L., P.G.S. and G.J.V. conceived the experiments. H.L. and G.B. performed the optomechanical measurements with heating control system. H.L. fabricated and inspected the samples. C.B.C. synthesized and characterized the FePS₃ crystals. H.L., G.J.V., P.G.S. and H.S.J.v.d.Z. analyzed and modeled the experimental data. H.S.J.v.d.Z. and P.G.S. supervised the project. The paper was jointly written by all authors with a main contribution from H.L. All authors discussed the results and commented on the paper.

Notes

The authors declare no competing financial interest.

Acknowledgement

P.G.S. and G.J.V. acknowledges support by the Dutch 4TU federation for the Plantenna project. H.L. acknowledges the financial support from China Scholarship Council. G.B., H.S.J.v.d.Z., and P.G.S. acknowledge funding from the European Union's Horizon 2020 research and innovation program under grant agreement no. 881603. C. B. C acknowledges the financial support from the European Union (ERC AdG Mol-2D 788222), the Spanish MICIN (2D-HETEROS PID2020-117152RB-100, co-financed by FEDER, and Excellence Unit "María de Maeztu" CEX2019-000919-M), the Generalitat Valenciana (PROMETEO Program and PO FEDER Program, Ph.D fellowship) and the Advanced Materials program (supported by MCIN with funding from European Union NextGenerationEU (PRTR-C17.I1) and by Generalitat Valenciana).

Supporting Information Available

Section 1: Mechanical buckling model for clamped circular membranes

1.1 Resonance frequency versus temperature

We consider a circular mechanical resonator, modeled as a membrane of radius R along the r axis, clamped on the Si/SiO₂ substrate (see Fig. S1). Under uniformly distributed compression, its mode shape ξ can be given as⁴³ $\xi(r) = \frac{z}{2}(1 - \cos(\frac{\pi r}{R} + \pi))$, where z is the central deflection of the membrane. The stored elastic energy U_{el} of the membrane, containing the contributions from tension and bending stiffness,²⁴⁻²⁶ is expressed as:

$$\begin{aligned} U_{el} &= U_{el \rightarrow tension} + U_{el \rightarrow Bending} \\ &= \frac{\pi Et}{1 - \nu^2} \int_0^R [\epsilon_0 + \frac{1}{2}\xi'^2(r)]^2 r dr + D\pi \int_0^R [(\xi''(r) + \frac{1}{r}\xi'(r))^2 - 2(1 - \nu)\xi''(r)(\frac{1}{r}\xi'(r))] r dr \\ &= \frac{\pi Et}{1 - \nu^2} (\frac{\epsilon_0^2 R^2}{2} + \frac{\pi^2 \epsilon_0 z^2}{16} + \frac{3\pi^4 z^4}{1024 R^2}) + D\pi (\frac{z^2 \pi^4}{16 R^2} + \frac{3z^2}{R^2}), \quad (S1) \end{aligned}$$

where t , E , and ν are the thickness, Young's modulus, and Poisson's ration of the membrane, respectively, D is the bending rigidity given by $D = \frac{Et^3}{12(1-\nu^2)}$, and ϵ_0 is the built-in strain. Accordingly, the spring constant of resonator $k_s = \frac{\partial^2 U_{el}}{\partial z^2}$ is:

$$k_s = \frac{\pi Et}{1 - \nu^2} (\frac{\pi^2 \epsilon_0}{8} + \frac{9\pi^4 z^2}{256 R^2} + \frac{t^2}{12} (\frac{\pi^4}{8 R^2} + \frac{6}{R^2})). \quad (S2)$$

Using the obtained k_s above, we find the fundamental resonance frequency $f_0 = \frac{1}{2\pi} \sqrt{\frac{k_s}{m_{\text{eff}}}}$ of the buckled mechanical resonator through:

$$f_0 = \frac{c_1}{2\pi R} \sqrt{\frac{E}{\rho(1 - \nu^2)} (\epsilon_0 + \frac{c_2 z^2}{R^2} + \frac{c_3 t^2}{R^2})}, \quad (S3)$$

where $m_{\text{eff}} = 0.297\pi R^2 \rho t$ is the effective mass of the fundamental mode of the resonator, and the constants are calculated as $c_1 = 2.0367$, $c_2 = 2.7758$ and $c_3 = 1.5147$. The factor 0.297

in m_{eff} is calculated using $2\pi \int_0^R \frac{\xi(r)}{z} r dr$.⁴⁴ Under thermally induced compression, Eq. S3 changes into:

$$f_0(T) = \frac{c_1}{2\pi R} \sqrt{\frac{E}{\rho(1-\nu^2)} \left(\epsilon_0 + \Delta\epsilon(T) + \frac{c_2 z(T)^2}{R^2} + \frac{c_3 t^2}{R^2} \right)}, \quad (\text{S4})$$

where $\Delta\epsilon(T) = -\int_{T_0}^T [\alpha_m(T) - \alpha_{\text{Si}}(T)] dT$ represents the compressive strain due to the thermal expansion, α_m and α_{Si} are the TECs of the membrane and Si substrate, respectively, and $z(T)$ is the central deflection of the membrane due to buckling. Eq. S4 corresponds to Eq. 2 in the main text, where we use r to represent the radius of the membrane in Eq. 2.

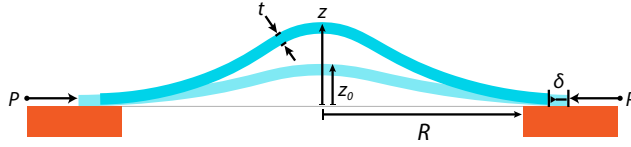


Figure S1: Schematic diagram of a clamped circular membrane under axially compressive load P , results in a central deflection z (cross-section view).

We assume that the initial and final deflection of the beam are small compared to its length and that the cross-sectional dimensions and amplitude of flexural vibration are small compared to the wavelength of the vibration.⁴⁵ In the presence of an axial load P (see Fig. S1), the membrane deflection becomes:

$$z = \frac{a_1 \xi_{c1}}{1 - \frac{P}{P_{c1}}} + \frac{a_2 \xi_{c2}}{1 - \frac{P}{P_{c2}}} + \dots + \frac{a_n \xi_{cn}}{1 - \frac{P}{P_{cn}}} + \dots, \quad (\text{S5})$$

where P_{cn} and ξ_{cn} are the n th critical buckling load and mode shape for flatted membrane, respectively, and $a_n = \int_{-R}^R \xi_0 \xi_{cn} dr / \int_{-R}^R \xi_{cn}^2 dr$. From literature, $P_{cn} = k_n D / R^2$, where k_n is a constant. Provided the initial deflection z_0 sufficiently resembles the first critical buckling mode, $\xi = a_1 \xi_{c1}$ and thus the mode shape under buckling is $\xi^* = \xi / (1 - P / P_{c1})$. Under the initial mode shape $\xi(r) = \frac{z_0}{2} (1 - \cos(\pi r / R + \pi))$, the axial displacement δ as P loaded is:

$$\delta = \frac{PR(1-\nu)}{Et} + \frac{\pi^2}{8R} (z^2 - z_0^2). \quad (\text{S6})$$

In the right hand side of Eq. S6, the first term denotes the axial compression of the membrane described by Hooke's law, while the second term with respect to the change of membrane's length is given by $\frac{1}{2}[\int_{-R}^R(\xi^{*'}(r)^2 - \xi'(r)^2)dr]$. Substituting $P_{c1} = k_1 D/R^2$ and $z = z_0/(1 - P/P_{c1})$ into Eq. S6, we have:

$$-\Delta\epsilon(T) = \delta/R = \left(1 - \frac{z_0}{z}\right) \frac{k_1 t^2 (1 + \nu)}{12R^2} + \frac{\pi^2}{8R^2} (z^2 - z_0^2), \quad (\text{S7})$$

where the first critical loading factor $k_1 = 14.68$.⁴⁶ We thus find that $z(T)$ is related to $\Delta\epsilon(T)$ and z_0 .

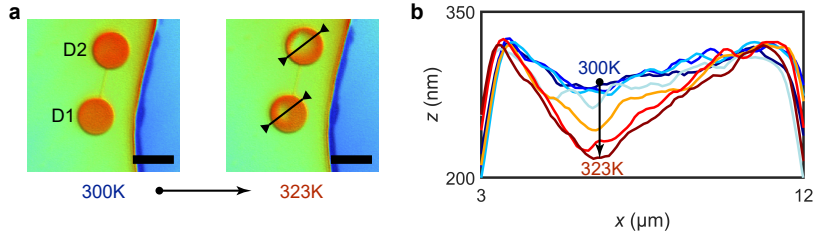


Figure S2: (a) Measurement results of FePS₃ nanoflake under white light interferometry. Left, 300 K; right, 323 K. Scale bar is 10 μm (b) Scanning of the surface profile of device D2 as temperature goes up from 300 K to 323 K, following the black line in (a). Corresponding result for device D1 is plotted in Figs. 3d and 3e in the main text.

Figure S2 shows the scanning results of FePS₃ devices D1 and D2 using white light interferometer. We observe that both of them buckle downwards as T increases from 300 K to 323 K (see Fig. S2a). T -dependent surface profile of devices D1 and D2 are shown in Figs. 3c and S2b, respectively. This also allows to extract the central deflection z of the membrane as the function of T . As depicted in Fig. 3e in the main text, the measured values of $z(T)$ are comparable to the estimation from mechanical buckling model.

1.2 Determining prestrain and initial deflection of 2D nanomechanical resonators

To keep the parameter consistence between the main text and this section, we redefine the radius of the membrane as r in the following discussion.

We now explain how to extract z_0 and ϵ_0 from the measured f_0 versus T . As introduced in the main text, we use two specific features: (i) at initial temperature $T = T_0$, $\Delta\epsilon(T_0) = 0$ and $z(T_0) = 0$; (ii) at turning temperature $T = T_t$, we have $\frac{\partial f_0}{\partial T}|_{T=T_t} = 0$. Firstly, we rewrite Eq. S4 as:

$$f_0^2(T) = \frac{1}{c_t} \left[\epsilon_0 + \Delta\epsilon(T) + \frac{c_2 z(T)^2}{r^2} + \frac{c_3 t^2}{r^2} \right], \quad (\text{S8})$$

where the constant $1/c_t = \left(\frac{c_1}{2\pi r}\right)^2 \frac{E}{\rho(1-\nu^2)}$. The relation between $\Delta\epsilon(T)$ and $z(T)$ is given by Eq. S7.

From condition (i) we find:

$$c_t f_0^2(T_0) = \epsilon_0 + \frac{c_2 z_0^2}{r^2} + \frac{c_3 t^2}{r^2}. \quad (\text{S9})$$

This gives us a direct relation between ϵ_0 and z_0 . From condition (ii), we find that the derivative of Eq. S8 is expressed as:

$$c_t \frac{\partial f_0^2(T)}{\partial T} = \frac{\partial \Delta\epsilon}{\partial z} \frac{\partial z}{\partial T} + 2c_2 \frac{z}{r^2} \frac{\partial z}{\partial T} = 0, \quad (\text{S10})$$

and thus:

$$\frac{\partial \Delta\epsilon}{\partial z} = -2c_2 \frac{z(T)}{r^2}. \quad (\text{S11})$$

Using the relation in Eq. S7, we find:

$$\frac{\partial \Delta\epsilon}{\partial z} = -\frac{\partial}{\partial z} \left[\left(1 - \frac{z_0}{z}\right) \frac{k_1 t^2 (1 + \nu)}{12r^2} + \frac{\pi^2}{8r^2} (z^2 - z_0^2) \right] = \frac{k_1 t^2 (1 + \nu)}{12r^2} \frac{z_0}{z^2} + \frac{\pi^2}{4r^2} z. \quad (\text{S12})$$

This results in a single equation for z at the turning temperature T_t by inserting Eq. S12 into Eq. S11:

$$\frac{k_1 t^2 (1 + \nu)}{12r^2} \frac{z_0}{z^2} + \frac{\pi^2}{4r^2} z = 2c_2 \frac{z}{r^2}, \quad (\text{S13})$$

which gives us a solution of z as:

$$z^3 = \frac{z_0 k_1 t^2 (1 + \nu)}{24(c_2 - \pi^2/8)}, \quad \text{or} \quad z(T_t) = \sqrt[3]{\eta z_0}, \quad (\text{S14})$$

with $\eta = \frac{k_1 t^2 (1 + \nu)}{24(c_2 - \pi^2/8)}$. At the turning temperature T_t , we thus have:

$$-\Delta\epsilon(T_t) = \left(1 - \sqrt[3]{\frac{z_0^2}{\eta}}\right) \frac{k_1 t^2 (1 + \nu)}{12r^2} + \frac{\pi^2}{8r^2} (\sqrt[3]{\eta^2 z_0^2} - z_0^2). \quad (\text{S15})$$

Using Eq. S14 and Eq. S15 in Eq. S8, we find a second equation (besides Eq. S9) that relates z_0 and ϵ_0 :

$$\begin{aligned} c_t f_0^2(T_b) &= \epsilon_0 + \Delta\epsilon(T_b) + \frac{c_2 z(T_b)^2}{r^2} + \frac{c_3 t^2}{r^2}, \\ &= \epsilon_0 + \frac{c_3 t^2}{r^2} + \frac{c_2 \sqrt[3]{\eta z_0}}{r^2} - \left(1 - \sqrt[3]{\frac{z_0^2}{\eta}}\right) \frac{k_1 t^2 (1 + \nu)}{12r^2} - \frac{\pi^2}{8r^2} (\sqrt[3]{\eta^2 z_0^2} - z_0^2). \end{aligned} \quad (\text{S16})$$

Note that in Eq. S9, ϵ_0 is already known in terms of z_0 . Therefore, combining Eq. S9 with Eq. S16, we can finally extract the expression of $z(T_t)$ as:

$$\frac{c_t [f_0^2(T_t) - f_0^2(T_0)]}{\left[\frac{c_2}{r^2} - \frac{\pi^2}{8r^2}\right]} = 3\sqrt[3]{\eta^2 z_0^2} - 2\eta - z_0^2. \quad (\text{S17})$$

Meanwhile, the prestrain ϵ_0 in the membrane can be also extracted from the measured $f_0(T_0)$ and $f_0(T_t)$. The symbol of resonance frequency $f_0(T_t)$ at the turning point is shorten as f_t in the main text.

Section 2: Thermal time constant of 2D nanomechanical resonators

Besides the primarily measured parameters as introduced in the main text, we plot here the obtained thermal time constant τ as the function of T for all devices D1–D5 in Fig. S3. τ

is extracted from the measured thermal signal using the fitting with Eq. 1 in the main text.

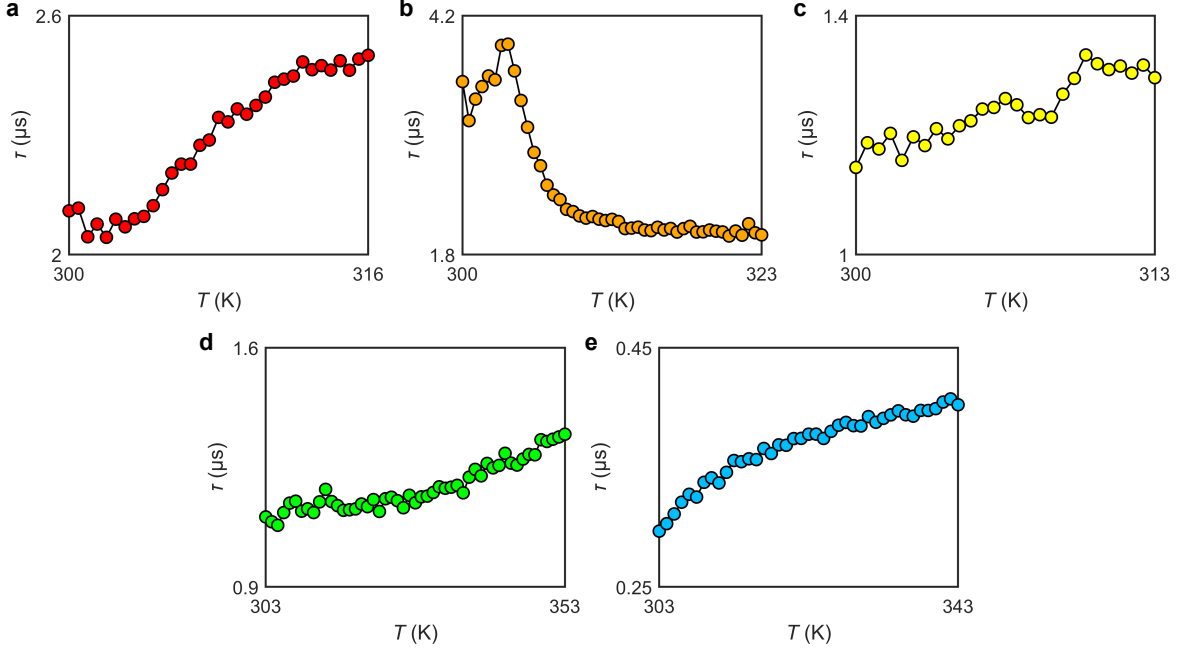


Figure S3: Measured thermal time constant τ as the function of temperature T for all devices. (a) FePS₃ device D2; (b) FePS₃ device D3; (c) 2H-TaS₂ device D4; (d) WSe₂ device D5.

Section 3: Enhanced photothermal response in 2D buckled resonators

In all optomechanical measurements, we observe an enhancement of both the resonance peak amplitude and thermal signal amplitude for all devices near the buckling bifurcation (Fig. 3 and 4 in the main text). Here, we theoretically analyse this relation between the amplitude $|A_{\text{res}}|$ at resonance ($f = f_0$) and that $|A_{\text{th}}|$ of thermal expansion ($f = \frac{1}{2\pi\tau}$).

Following the literature,⁴⁷ the motion, A_f , of a oscillator driven by the laser-induced thermal expansion can be expressed as:

$$\begin{cases} \text{Re}(A_f) = \frac{\varepsilon_\omega F_{th}}{m_{\text{eff}}} \frac{\omega_0^2 - \omega^2(1 + \Gamma\tau)}{[(\omega_0^2 - \omega^2)^2 + \omega^2\Gamma^2](1 + \omega^2\tau^2)}, \\ \text{Im}(A_f) = \frac{\varepsilon_\omega F_{th}}{m_{\text{eff}}} \frac{-\omega[(\omega_0^2 - \omega^2)\tau + \Gamma]}{[(\omega_0^2 - \omega^2)^2 + \omega^2\Gamma^2](1 + \omega^2\tau^2)}, \end{cases} \quad (\text{S18})$$

where m_{eff} is the effective mass of the fundamental mode, ε_ω is a small modulation strength describes the perturbation of driven force in time domain, F_{th} is thermal driven force, $\Gamma = \frac{\omega_0}{Q}$ is the damping of oscillator, $\omega = 2\pi f$ and $\omega_0 = 2\pi f_0$. The absolute value of A_ω can be obtained by Eq. S18. As a result, the amplitude ratio between thermal signal ($|A_{\text{th}}|$) and resonance peak ($|A_{\text{res}}|$) is expressed as $\beta = \frac{A_f|_{f=1/(2\pi\tau)}}{A_f|_{f=f_0}}$. We estimate $|A_{\text{th}}|$ using the measured f_0 , Q , τ and $|A_{\text{res}}|$, of which the T -dependence is consistent with the measured $|A_{\text{th}}|$ for all devices D1–D5 (see Figs. 3g and 4c in the main text).

References

- (1) Hu, N.; Burgueño, R. Buckling-induced smart applications: recent advances and trends. *Smart Materials and Structures* **2015**, *24*, 063001.
- (2) Lindahl, N.; Midtvedt, D.; Svensson, J.; Nerushev, O. A.; Lindvall, N.; Isacson, A.; Campbell, E. E. Determination of the bending rigidity of graphene via electrostatic actuation of buckled membranes. *Nano letters* **2012**, *12*, 3526–3531.
- (3) Le Doussal, P.; Radzihovsky, L. Thermal buckling transition of crystalline membranes in a field. *Physical Review Letters* **2021**, *127*, 015702.
- (4) El Mansouri, B.; Middelburg, L. M.; Poelma, R. H.; Zhang, G. Q.; van Zeijl, H. W.; Wei, J.; Jiang, H.; Vogel, J. G.; van Driel, W. D. High-resolution MEMS inertial sensor combining large-displacement buckling behaviour with integrated capacitive readout. *Microsystems & nanoengineering* **2019**, *5*, 1–14.
- (5) Kim, S.; Bunyan, J.; Ferrari, P. F.; Kanj, A.; Vakakis, A. F.; Van Der Zande, A. M.; Tawfick, S. Buckling-mediated phase transitions in nano-electromechanical phononic waveguides. *Nano letters* **2021**, *21*, 6416–6424.
- (6) Rechnitz, S.; Tabachnik, T.; Shlafman, S.; Shlafman, M.; Yaish, Y. E. DC Signature

- of Snap-through Bistability in Carbon Nanotube Mechanical Resonators. *Nano Letters* **2022**, *22*, 7304–7310.
- (7) Kanj, A.; Ferrari, P. F.; van der Zande, A. M.; Vakakis, A. F.; Tawfick, S. Ultra-tuning of nonlinear drumhead MEMS resonators by electro-thermoelastic buckling. *arXiv preprint arXiv:2210.06982* **2022**,
- (8) Zhang, W.; Yan, H.; Peng, Z.; Meng, G. Electrostatic pull-in instability in MEMS/NEMS: A review. *Sensors and Actuators A: Physical* **2014**, *214*, 187–218.
- (9) Harne, R. L.; Wang, K. A review of the recent research on vibration energy harvesting via bistable systems. *Smart materials and structures* **2013**, *22*, 023001.
- (10) Xu, B.; Zhang, P.; Zhu, J.; Liu, Z.; Eichler, A.; Zheng, X.-Q.; Lee, J.; Dash, A.; More, S.; Wu, S., et al. Nanomechanical resonators: toward atomic scale. *ACS nano* **2022**, *16*, 15545–15585.
- (11) Steeneken, P. G.; Dolleman, R. J.; Davidovikj, D.; Alijani, F.; Van der Zant, H. S. Dynamics of 2D material membranes. *2D Materials* **2021**, *8*, 042001.
- (12) Liu, H.; Basuvalingam, S. B.; Lodha, S.; Bol, A. A.; van der Zant, H. S.; Steeneken, P. G.; Verbiest, G. Nanomechanical resonators fabricated by atomic layer deposition on suspended 2D materials. *arXiv preprint arXiv:2212.08449* **2022**,
- (13) Iguñiz, N.; Frisenda, R.; Bratschitsch, R.; Castellanos-Gomez, A. Revisiting the buckling metrology method to determine the Young’s modulus of 2D materials. *Advanced Materials* **2019**, *31*, 1807150.
- (14) Kim, S. Impact of the van der Waals interface on the mechanics of 2D nanoelectromechanical systems. Ph.D. thesis, University of Illinois at Urbana-Champaign, 2020.
- (15) Ferrari, P. F.; Kim, S.; Van Der Zande, A. M. Dissipation from interlayer friction in graphene nanoelectromechanical resonators. *Nano letters* **2021**, *21*, 8058–8065.

- (16) Castellanos-Gomez, A.; Poot, M.; Steele, G. A.; Van Der Zant, H. S.; Agraït, N.; Rubio-Bollinger, G. Elastic properties of freely suspended MoS₂ nanosheets. *Advanced materials* **2012**, *24*, 772–775.
- (17) Lee, M.; Šiškins, M.; Mañas-Valero, S.; Coronado, E.; Steeneken, P. G.; van der Zant, H. S. Study of charge density waves in suspended 2H-TaS₂ and 2H-TaSe₂ by nanomechanical resonance. *Applied Physics Letters* **2021**, *118*, 193105.
- (18) Šiškins, M.; Lee, M.; Mañas-Valero, S.; Coronado, E.; Blanter, Y. M.; van der Zant, H. S.; Steeneken, P. G. Magnetic and electronic phase transitions probed by nanomechanical resonators. *Nature communications* **2020**, *11*, 1–7.
- (19) Zhang, R.; Koutsos, V.; Cheung, R. Elastic properties of suspended multilayer WSe₂. *Applied Physics Letters* **2016**, *108*, 042104.
- (20) Šiškins, M.; Sokolovskaya, E.; Lee, M.; Mañas-Valero, S.; Davidovikj, D.; Van Der Zant, H. S.; Steeneken, P. G. Tunable strong coupling of mechanical resonance between spatially separated FePS₃ nanodrums. *Nano letters* **2021**, *22*, 36–42.
- (21) Dolleman, R. J.; Lloyd, D.; Lee, M.; Bunch, J. S.; Van Der Zant, H. S.; Steeneken, P. G. Transient thermal characterization of suspended monolayer MoS₂. *Physical Review Materials* **2018**, *2*, 114008.
- (22) Liu, H.; Lee, M.; Šiškins, M.; van der Zant, H.; Steeneken, P.; Verbiest, G. Tension tuning of sound and heat transport in graphene. *arXiv preprint arXiv:2204.06877* **2022**,
- (23) Hajjaj, A.; Jaber, N.; Ilyas, S.; Alfossail, F.; Younis, M. I. Linear and nonlinear dynamics of micro and nano-resonators: Review of recent advances. *International Journal of Non-Linear Mechanics* **2020**, *119*, 103328.
- (24) Bouwstra, S.; Geijselaers, B. On the resonance frequencies of microbridges. Dig. Tech. Papers 6th Int. Conf. Solid-State Sensors and Actuators. 1991; pp 24–27.

- (25) Sajadi, B.; Alijani, F.; Davidovikj, D.; Goosen, J.; Steeneken, P. G.; van Keulen, F. Experimental characterization of graphene by electrostatic resonance frequency tuning. *Journal of Applied Physics* **2017**, *122*, 234302.
- (26) Chen, C.; Rosenblatt, S.; Bolotin, K. I.; Kalb, W.; Kim, P.; Kymissis, I.; Stormer, H. L.; Heinz, T. F.; Hone, J. Performance of monolayer graphene nanomechanical resonators with electrical readout. *Nature nanotechnology* **2009**, *4*, 861–867.
- (27) Hong, G.; Wang, C.; Tan, T. Analytical buckling solutions for circular Mindlin plates: inclusion of inplane prebuckling deformation. *Archive of Applied Mechanics* **1993**, *63*, 534–542.
- (28) Sha, Z.-D.; Pei, Q.-X.; Ding, Z.; Jiang, J.-W.; Zhang, Y.-W. Mechanical properties and fracture behavior of single-layer phosphorene at finite temperatures. *Journal of Physics D: Applied Physics* **2015**, *48*, 395303.
- (29) Lee, J.; Wang, Z.; He, K.; Shan, J.; Feng, P. X.-L. High frequency MoS₂ nanomechanical resonators. *ACS nano* **2013**, *7*, 6086–6091.
- (30) Takano, Y.; Arai, N.; Arai, A.; Takahashi, Y.; Takase, K.; Sekizawa, K. Magnetic properties and specific heat of MPS₃ (M= Mn, Fe, Zn). *Journal of Magnetism and Magnetic Materials* **2004**, *272*, E593–E595.
- (31) Dolleman, R. J.; Davidovikj, D.; Van Der Zant, H. S.; Steeneken, P. G. Amplitude calibration of 2D mechanical resonators by nonlinear optical transduction. *Applied Physics Letters* **2017**, *111*, 253104.
- (32) Bonilla, L.; Ruiz-Garcia, M. Critical radius and temperature for buckling in graphene. *Physical Review B* **2016**, *93*, 115407.
- (33) Nicholl, R. J.; Conley, H. J.; Lavrik, N. V.; Vlassiouk, I.; Puzyrev, Y. S.; Sreeni-

- vas, V. P.; Pantelides, S. T.; Bolotin, K. I. The effect of intrinsic crumpling on the mechanics of free-standing graphene. *Nature communications* **2015**, *6*, 1–7.
- (34) Wang, Z.; Yang, R.; Feng, P. X.-L. Thermal hysteresis controlled reconfigurable MoS₂ nanomechanical resonators. *Nanoscale* **2021**, *13*, 18089–18095.
- (35) Ye, F.; Lee, J.; Feng, P. X.-L. Electrothermally tunable graphene resonators operating at very high temperature up to 1200 K. *Nano Letters* **2018**, *18*, 1678–1685.
- (36) Davidovikj, D.; Groenendijk, D. J.; Monteiro, A. M. R.; Dijkhoff, A.; Afanasiev, D.; Šiškins, M.; Lee, M.; Huang, Y.; van Heumen, E.; van der Zant, H., et al. Ultrathin complex oxide nanomechanical resonators. *Communications Physics* **2020**, *3*, 163.
- (37) Lake Shore Ultra-Low Temperature Rox™. <https://qd-uki.co.uk/lake-shore/temperature-sensors/ultra-low-temperature-rox/>, March 16, 2023.
- (38) Blaikie, A.; Miller, D.; Alemán, B. J. A fast and sensitive room-temperature graphene nanomechanical bolometer. *Nature communications* **2019**, *10*, 4726.
- (39) Qian, Z.; Hui, Y.; Liu, F.; Kang, S.; Kar, S.; Rinaldi, M. Graphene–aluminum nitride NEMS resonant infrared detector. *Microsystems & nanoengineering* **2016**, *2*, 1–7.
- (40) Sarafraz, A.; Givois, A.; Roslon, I.; Liu, H.; Brahmi, H.; Verbiest, G.; Steeneken, P. G.; Alijani, F. Dynamics of pressurized ultra-thin membranes. *arXiv preprint arXiv:2212.05464* **2022**,
- (41) Verbiest, G. J.; Kirchhof, J. N.; Sonntag, J.; Goldsche, M.; Khodkov, T.; Stampfer, C. Detecting ultrasound vibrations with graphene resonators. *Nano letters* **2018**, *18*, 5132–5137.
- (42) Ramos, M.; Carrascoso, F.; Frisenda, R.; Gant, P.; Mañas-Valero, S.; Esteras, D. L.; Baldoví, J. J.; Coronado, E.; Castellanos-Gomez, A.; Calvo, M. R. Ultra-broad spectral

- photo-response in FePS3 air-stable devices. *npj 2D Materials and Applications* **2021**, *5*, 1–9.
- (43) Kim, C.; Dickinson, S. The flexural vibration of slightly curved slender beams subject to axial end displacement. *Journal of sound and vibration* **1986**, *104*, 170–175.
- (44) Weber, P.; Guttinger, J.; Tsioutsios, I.; Chang, D. E.; Bachtold, A. Coupling graphene mechanical resonators to superconducting microwave cavities. *Nano letters* **2014**, *14*, 2854–2860.
- (45) Dickinson, S. The lateral vibration of slightly bent slender beams subject to prescribed axial end displacement. *Journal of Sound and Vibration* **1980**, *68*, 507–514.
- (46) Williams, M.; Griffin, B.; Homeijer, B.; Sankar, B.; Sheplak, M. The nonlinear behavior of a post-buckled circular plate. *SENSORS*, 2007 IEEE. 2007; pp 349–352.
- (47) Metzger, C.; Favero, I.; Ortlieb, A.; Karrai, K. Optical self cooling of a deformable Fabry-Perot cavity in the classical limit. *Physical Review B* **2008**, *78*, 035309.